

## Systematic comparisons among OpenFAST, Charm3D-FAST simulations and DeepCWind model test for 5 MW OC4 semisubmersible offshore wind turbine

Jieyan Chen<sup>1</sup>, Chungkuk Jin<sup>2</sup> and Moo-Hyun Kim<sup>\*1</sup>

<sup>1</sup>*Department of Ocean Engineering, Texas A&M University, College Station, TX 77084, USA*

<sup>2</sup>*Department of Ocean Engineering and Marine Science, Florida Institute of Technology, Melbourne, FL 32901, USA*

(Received April 2, 2023, Revised May 25, 2023, Accepted June 2, 2023)

**Abstract.** Reliable prediction of the motion of FOWT (floating offshore wind turbine) and associated mooring line tension is important in both design and operation/monitoring processes. In the present study, a 5MW OC4 semisubmersible wind turbine is numerically modeled, simulated, and analyzed by the open-source numerical tool, OpenFAST and in-house numerical tool, Charm3D-FAST. Another commercial-level program FASTv8-OrcaFlex is also introduced for comparison for selected cases. The three simulation programs solve the same turbine-floater-mooring coupled dynamics in time domain while there exist minor differences in the details of the program. Both the motions and mooring-line tensions are calculated and compared with the DeepCWind 1/50 scale model-testing results. The system identification between the numerical and physical models is checked through the static-offset test and free-decay test. Then the system motions and mooring tensions are systematically compared among the simulated results and measured values. Reasonably good agreements between the simulation and measurement are demonstrated for (i) white-noise random waves, (ii) typical random waves, and (iii) typical random waves with steady wind. Based on the comparison between numerical results and experimental data, the relative importance and role of the differences in the numerical methodologies of those three programs can be observed and interpreted. These comparative-study results may provide a certain confidence level and some insight of potential variability in motion and tension predictions for future FOWT designs and applications.

**Keywords:** 5 MW OC4 semisubmersible; free-decay tests; random waves; responses and tensions; second-order wave forces; simulation vs experiment; turbine-hull-mooring coupled dynamics

### 1. Introduction

Global climate change and environmental crisis have threatened human health and safety. The overuse of fossil fuels may be related to the crisis. In this regard, many countries are moving toward the use of clean renewable energy in various industries and developments. Offshore wind energy is considered as one of the most affordable clean renewable energies. However, offshore wind turbine systems have to be operated in complex marine environments and survive severe sea storms. In water depth deeper than 50 m, FOWT (floating offshore wind turbine) is preferred. Its monitoring

---

\*Corresponding author, Professor, E-mail: m-kim3@tamu.edu

is also very challenging due to the limited observability and accessibility. Therefore, the development of a remote monitoring method with the help of digital twins and essential sensors is very important. In this regard, the development of a reliable digital twin of the unmanned FOWT is of high demand.

FOWT dynamics include complex hull-mooring-tower-RNA (rotor nacelle assembly) dynamic coupling with active control, so need to be solved in time domain. The fully coupled dynamic analysis of the moored floating turbine in random waves is still an active research area. Numerical studies proved that ignoring the coupling effect between the floating structure and mooring system would result in unreliable motion results (Ma *et al.* 2000, Lee and Flory 1999, Kim *et al.* 2001). For the simulation of offshore wind turbines. Masciola *et al.* (2013) analyzed the system by including only linear wave force and using quasi-static or lumped-mass methods for the mooring model. Also, Coulling *et al.* (2013a, b) performed the simulation for a semi-submersible platform including second-order wave-diffraction forces and Newman's approximation. However, the mooring model in the analysis was also quasi-static, so the true dynamic coupling with mooring lines was missing in the study. Besides, the second-order wave-diffraction force itself was by Newman's approximation method. Recently, Koo *et al.* (2014a) analyzed the dynamics of OC4 semisubmersible wind turbine and compared their numerical predictions by their own code, MLTSIM-FAST against DeepCWind model test results. Moreover, the second-order wave-diffraction effects were briefly introduced and discussed in their work (Koo *et al.* 2014b). On the other hand, Zhao and Wan carried out motion simulations of the OC4 semi-submersible platform in waves by using their own CFD code, NAOE-FOAM-SJTU (Zhao and Wan 2015). In Kim and Kim (2015), the fully coupled wind-turbine/hull/mooring dynamics of the OC4 semi-submersible model were calculated by including viscous and second-order difference-frequency wave effects with FE (finite element)-based mooring dynamics module.

An important aspect of the hydrodynamic analysis of the FOWT is to quantify the nonlinear effect involved. Although the force generated by nonlinear wave-wave and wave-body interactions is relatively small when compared with the wave-frequency excitation forces, these second-order forces may contribute at the structure's surge and pitch natural frequencies, which may result in large slowly-varying drift motions. Li and Zhang (2016) revealed and quantified nonlinear effects in the motion predictions of an offshore platform by quasi-static analysis with nonlinearity up to the second order in wave steepness. A similar study was also carried out by Chen (2006) in the dynamic analysis of a spar with mooring lines, which also indicated the importance of the second-order nonlinearity in the motion of the platform. However, it would still be interesting to analyze and quantify the nonlinear wave forces and their effects in the case of offshore wind turbines since its coupling effects are more complex than typical moored floating oil/gas platforms. A good review of different numerical tools and methods in the simulation of FOWTs can be found in Chen and Kim (2022).

In the present study, an in-house time-domain fully-coupled dynamic simulation program "Charm3D-FAST" (Bae and Kim 2011, 2014, Kim and Kim 2015, 2016) is used for the simulation of the OC4 semisubmersible wind turbine and its mooring system and the simulated results are systematically compared with DeepCWind 1/50-scale model test results. The wave forces acting on the structure under irregular wave conditions are calculated using the first- and second-order diffraction/radiation potential theory. The nonlinear viscous drag forces were calculated from Morison's formula at the instantaneous body position and up to the instantaneous free-surface elevation. The computation of the mooring system dynamics is based on a higher-order rod Finite Element Method (FEM). Similar time-domain simulations were also conducted by two widely used

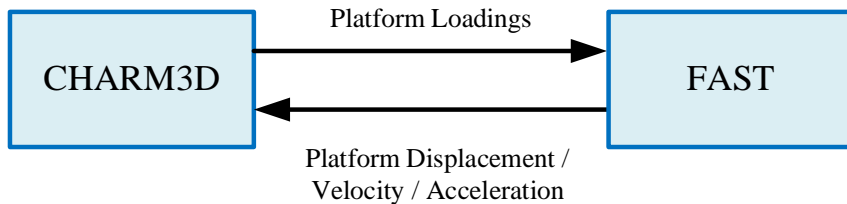


Fig. 1 Basic concept of CHARM3D-FAST coupling

commercial-level programs, OpenFAST and FASTv8-OrcaFlex, and their results are also systematically compared with the present Charm3D-FAST results. It is found that all the three computer programs can reasonably reproduce the physical model-testing results despite minor differences in the details of the programming and parameters inside.

## 2. Methodology

### 2.1 Numerical simulation in time domain

In order to solve the dynamics of a wind turbine on a single floating platform, the open-source program FAST (e.g., Jonkman and Buhl Jr. 2004) was developed by National Renewable Energy Laboratory (NREL) and has been modified and extended so that it can more accurately calculate the fully coupled dynamics among wind turbine, floating platform, and mooring lines. The coupled dynamic response between the turbine and floater can be derived from the full-degree-of-freedom (DOF) matrix equation including floater 6-DOFs and wind-turbine DOFs with their cross-coupling terms. The combined left-hand-side full matrix is solved with the given forcing functions in the right-hand side at each time step. In the present numerical modeling, every DOF for a three-bladed turbine in FAST is turned on, which includes 6 DOFs (for floater) + 18 DOFs (for turbine) making the total DOFs = 24. The coupled terms between the floating platform and turbine in the coefficient matrix can be derived by accounting for every effect of generalized inertia and active forces from both bodies. The detailed theory and equations are given in Bae and Kim (2014).

Between the floater and mooring line dynamics, the necessary data exchange is also done at each time step for their dynamic coupling. The hydro-dynamic loadings and instantaneous mooring responses and tensions are obtained from rod-element-based high-order FE (finite element) line dynamics program in CHARM3D (e.g., Kim *et al.* 2001, Tahar and Kim 2003, Yang and Kim 2010, Kim and Kim 2016, Kim *et al.* 2019, Jang *et al.* 2019) along with viscous drag forces on the instantaneous positions of Morison members and convolution-integral forces for a floater. They are fed to FAST at each time step. The transferred external forces also include first-order and second-order wave forces. Then FAST fills out the forcing function of the platform DOFs using those transferred forces, and solves displacements, velocities, and accelerations of all DOFs including elastic responses of towers and blades. The obtained platform displacement and velocity data are then fed into CHARM3D side to update the external forces. The instantaneous velocities of the platform are used for the next-time-step convolution–integral term. The instantaneous positions of

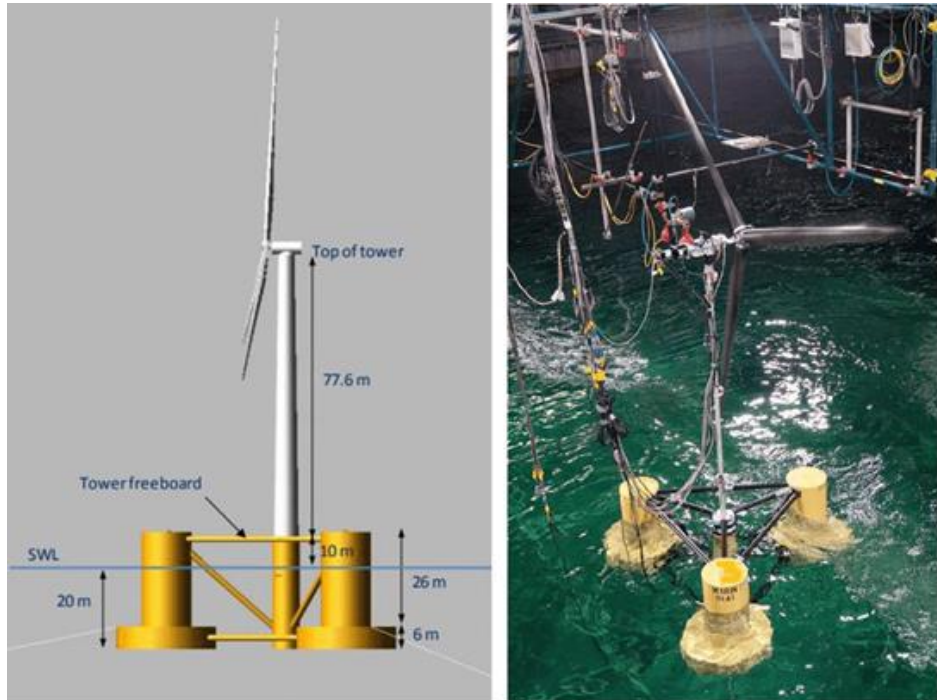


Fig. 2 DeepCWind semisubmersible (Jonkman *et al.* 2007) (Left) and Image of 1/50th-scale model test of the DeepCWind OC4-semi (Coulling *et al.* 2013) (Right)

the platform's Morison members are used for viscous drag forces with instantaneous incident-wave kinematics. The transferred instantaneous positions of the mooring-connection points are used as an input for the next-time-step mooring dynamics. The basic concept of rotor-floater coupling is schematically shown in Fig. 1. Fig. 2 shows the pictures of the entire 5MW OC4-semi wind turbine and the corresponding experimental setup.

## 2.2 Second-order wave loads and convolution integral in time domain

In this section, the time-domain realization of the first- and second-order wave forces/momenta in a random sea environment is explained. The first- and second-order hydrodynamic forces/momenta on a body caused by stationary Gaussian random waves can be written as a two-term Volterra series in the time domain as follows

$$F^{(1)}(t) + F^{(2)}(t) = \int_{-\infty}^{\infty} h_1(\tau) \eta(t - \tau) d\tau + \int_{-\infty}^{\infty} \int_{-\infty}^{\infty} h_2(\tau_1, \tau_2) \eta(t - \tau_1) \eta(t - \tau_2) d\tau_1 d\tau_2 \quad (1)$$

where  $\eta(t)$  is the incident wave free surface elevation at a reference position,  $h_1(\tau)$  is the linear impulse force function, and  $h_2(\tau_1, \tau_2)$  is the quadratic impulse force function. The above equation can also be expressed in the form of the summation of  $N$  frequency component waves as below

$$F_I^{(1)}(t) = \text{Re} \left[ \sum_{j=1}^N A_j L(\omega_j) e^{i\omega_j t} \right] \quad (2)$$

Table 1 DeepCwind Semisubmersible platform property

| Item                              | Unit              | Value      |
|-----------------------------------|-------------------|------------|
| Platform Center of Mass           | m                 | -14.4      |
| Platform Mass                     | ton               | 1.3444E+04 |
| Platform Inertia $I_{xx}, I_{yy}$ | kg·m <sup>2</sup> | 8.0110E+09 |
| Platform Inertia $I_{zz}$         | kg·m <sup>2</sup> | 1.3910E+10 |
| Nacelle and blade Mass            | ton               | 397.1      |
| Tower Mass                        | ton               | 302.2      |

$$F_I^{(2)}(t) = \text{Re} \left[ \sum_{j=1}^N \sum_{k=1}^N A_j A_k^* D(\omega_j, -\omega_k) e^{i\omega^- t} \right] \quad (3)$$

where  $L(\omega_j)$  represents the linear force transfer function (LTF),  $A_j$  is component wave amplitudes, and  $D(\omega_j, -\omega_k)$  is the difference-frequency quadratic-force transfer function (QTF). Eq. (3) represents the difference-frequency ( $\omega^-$ ) second-order forces/momenta. The sum-frequency second-order forces/momenta are not included since they play little role in the overall dynamics of a semisubmersible platform. On the other hand,  $F_I^{(2)}(t)$  can be rewritten by Newman's approximation as follows

$$F_I^{(2)}(t) = \text{Re} \left[ \sum_{j=1}^N \sum_{k=1}^N A_j A_k^* D \left( \frac{\omega_j + \omega_k}{2}, \frac{\omega_j + \omega_k}{2} \right) e^{i\omega^- t} \right] \quad (4)$$

The radiation-potential-induced force/moment in time domain can be expressed as follows

$$F_R(t) = -M^a(\infty) \ddot{\zeta}(t) - \int_{-\infty}^t R(t - \tau) \dot{\zeta}(\tau) d\tau \quad (5)$$

where  $\zeta$  is platform motion, an upper dot denotes time derivative,  $M^a(\infty)$  is the added mass of the platform at infinite frequency, and  $R(t)$  is the retardation function or time-memory function, which is related to the frequency-domain solutions of the radiation problem as follows

$$R(t) = \frac{2}{\pi} \int_0^\infty C(\omega) \frac{\sin \omega t}{\omega} d\omega \quad (6)$$

where  $C(\omega)$  is the radiation-wave-induced damping coefficient at frequency  $\omega$ . The total wave loads in time domain can then be written by summing all the force components as below.

$$F_{total}(t) = F_I(t) + F_R(t) \quad (7)$$

### 2.3 DeepCWind semisubmersible wind-turbine model description

Table 1 and Fig. 3 show the 5MW OC4 semisubmersible floating platform properties and geometries used for DeepCwind model testing (Coulling *et al.* 2013). The property in Table 1 is only for the floating platform and the wind turbine part is not included. The wind turbine is based on NREL 5 MW baseline turbine (Jonkman *et al.* 2007) but it is modified for a 1/50-scale model test (Coulling *et al.* 2013).

### 2.4 Numerical modeling

3600 panels are used on the half of the wet hull according to  $x$ -axis symmetry, with finer modeling

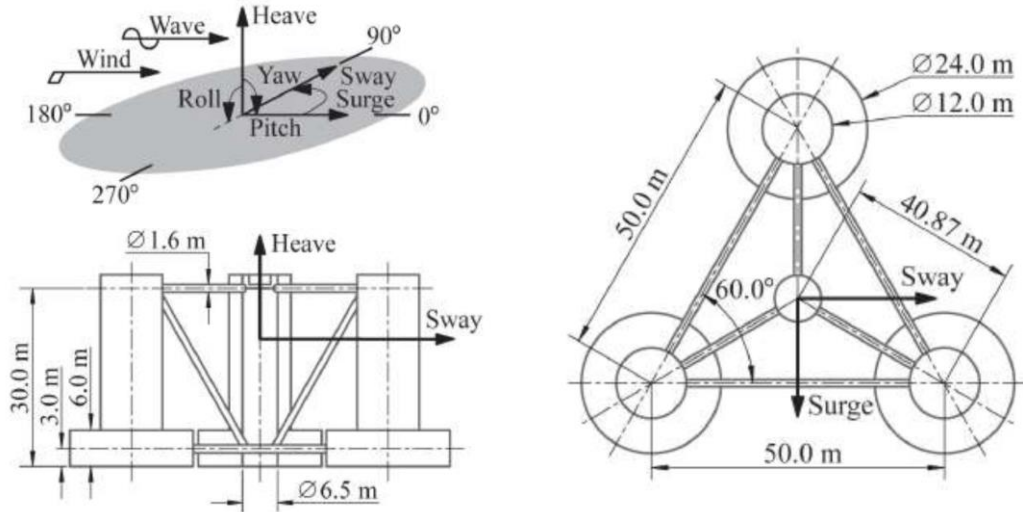


Fig. 3 DeepCwind Semisubmersible platform geometry front view (Left) and top view (Right) (Coulling *et al.* 2013)

near free surface, as illustrated in Fig. 4. Furthermore, free-surface discretization is necessary to solve the complete second-order diffraction/radiation problem (Kim and Yue 1989, 1990). The free-surface discretization was performed using 4888 panels up to an 80-meter truncated radius (Kim and Kim 2015). Only the second-order difference-frequency force is considered in the present application since the sum-frequency part plays little role. The WAMIT program first calculates the potential-based hydrodynamic coefficients and excitations in frequency domain, and they are subsequently used for time-domain simulations for Charm3D-FAST. In the present study, we also applied the Morison equation to account for the viscous drag force on the Morison members including the braces that connect columns and pontoons. Having relative velocities squared in the equation, the drag forces on Morison members contribute to both excitation and damping. The viscous drag forces on Morison members above MWL are evaluated using the instantaneous wave kinematics uniformly extrapolated from the values at MWL. Nonlinear viscous drag forces also contribute to higher harmonics because they are evaluated at the instantaneous platform positions. In potential forces, all diffraction-radiation components are included up to the second order.

The wind turbine model adopted is the offshore 5 MW baseline wind turbine from the National Renewable Energy Laboratory (NREL). In the present study, we focus on the numerical hydrodynamics modeling of the floating foundation; the flexibility option for the blades was turned off. The tower's flexibility is represented by a linear modal representation. The coupled dynamic analysis of hull-turbine-mooring used two fore-aft and two side-to-side tower modes. The natural frequencies of the lowest fore-aft and side-to-side modes of the tower are 2.20 and 2.39 rad/sec, respectively (Coulling *et al.* 2013a). These natural frequencies are much higher than the wave frequency and the 6DOFs hull natural frequencies. A detailed description of the tower-blade-control models can be found in Bae and Kim (2014). The flexibility of the tower plays much less role in overall coupled dynamics of the present semisubmersible floater than TLP floating foundation (Bae and Kim 2011).

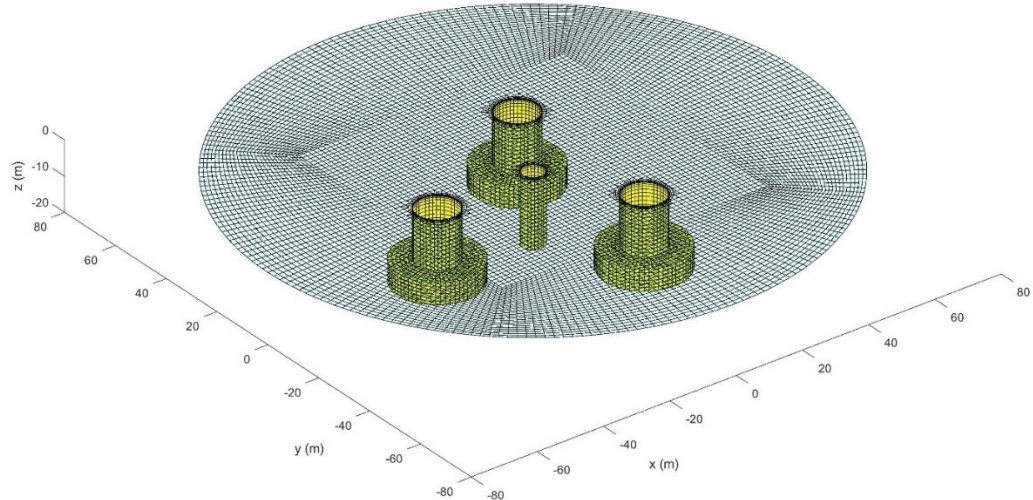


Fig. 4 WAMIT model with body and free surface panels for potential-flow calculation

Table 2 Vertical-plane static equilibrium

|                             |             |
|-----------------------------|-------------|
| Platform + Tower Weight (N) | 1.38703E+08 |
| Buoyancy (N)                | 1.40589E+08 |
| Total Vertical Tension (N)  | 1.88612e+06 |

Table 3 Anchor points

|                 |                       |
|-----------------|-----------------------|
| #1 Anchor Point | (418.8, 725.4, -200)  |
| #2 Anchor Point | (-837.6, 0, -200)     |
| #3 Anchor Point | (418.8, -725.4, -200) |

Table 4 Mooring properties

|                                 |        |        |
|---------------------------------|--------|--------|
| Mooring Axial Stiffness         | $MN$   | 753.6  |
| Unstretched Mooring Line Length | $M$    | 835.5  |
| Mooring Mass Density (Dry)      | $kg/m$ | 113.35 |
| Mooring Mass Density (Wet)      | $kg/m$ | 108.63 |
| Seabed Friction Coefficient     | -      | 1      |
| Mooring Drag Coefficient        | -      | 2.4    |
| Mooring Added-Mass Coefficient  | -      | 1      |

The mooring system consists of three catenary lines that are omni-spread. The Charm3D's preprocessor HARP was used to model mooring lines. As shown in Table 2, the buoyancy of the platform must be equal to the sum of the weight of the entire structure plus the vertical component tension of the mooring system to maintain static equilibrium. The mooring dynamics are modeled using the high-order finite rod-element method, which is detailed in Kim *et al.* (2001) and Tahar and

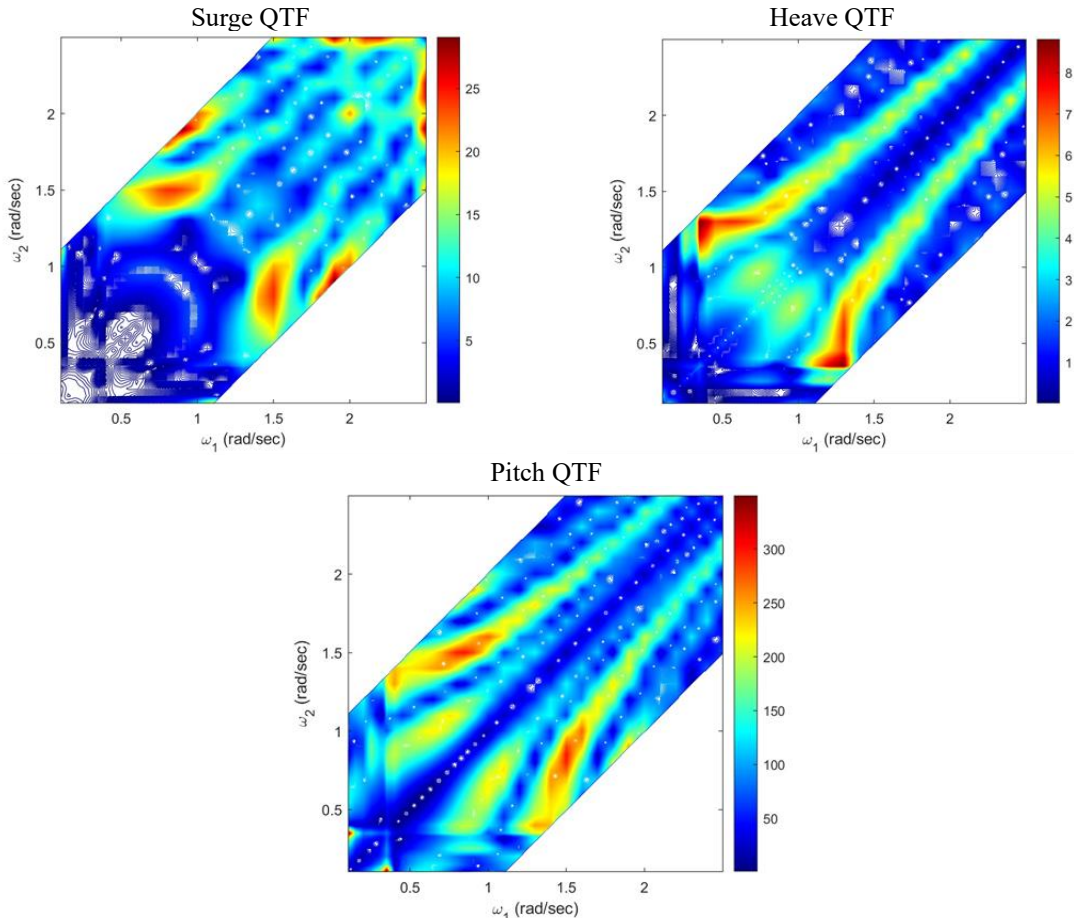


Fig. 5 Difference-frequency wave-force QTFs for surge (Top-left), heave (Top-right), and pitch (Bottom) plotted in the bi-frequency domain

Kim (2003). The drag coefficient used for the chain mooring was 2.4. Table 3 shows the anchor points, while Table 4 displays the mooring line properties. The mooring system is correctly modeled according to the comparison of physical/numerical static offset tests (see Fig. 6 of Kim and Kim 2015).

Fig. 5 shows the difference-frequency wave force QTFs for surge, heave, and pitch modes plotted in the bi-frequency domain. The diagonals represent mean surge-heave-pitch drift forces and moment. The QTF should be symmetric with respect to the diagonal, as can be seen in the figure. The second-order difference-frequency surge forces are in general larger than those heave forces. There exist local peaks near (1.0 & 1.5 rad/s) pair in the surge and pitch. Since surge and pitch natural frequencies are 0.05 rad/s and 0.24 rad/s (see Table 6), the respective QTF magnitudes of that much distance from the diagonal become important. The QTFs were calculated from the second-order WAMIT diffraction/radiation program at 0.05 rad/sec frequency interval at low-frequency range and 0.1 rad/s frequency interval at wave-frequency range. The other values were linearly interpolated.

The same QTF results given in Fig. 5 and the same other potential-theory results were inputted for the three simulation programs for a fair comparison.

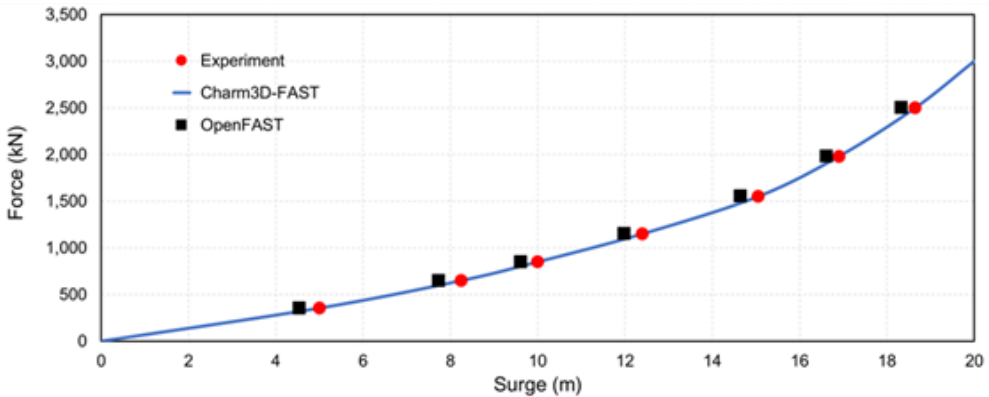


Fig. 6 Surge Static offset tests by experiment, Charm3D-FAST and OpenFAST

## 2.5 OpenFAST simulation tool

To validate and assess our in-house numerical simulation tool Charm3D-FAST, we also utilized the OpenFAST tool of NREL in the present study. OpenFAST is a multi-physics, multi-fidelity tool for simulating the coupled dynamic responses of wind turbines. OpenFAST is the “glue code” that couples computational modules for aerodynamics (AeroDyn), hydrodynamics (HydroDyn), control-electrical system (ServoDyn) dynamics, and structural dynamics (ElastoDyn) to enable coupled nonlinear aero-hydro-servo-elastic simulation in the time domain.

The HydroDyn module gives the hydrodynamic loads and motions of the floating platform. These loads include the potential-flow solution and strip-theory solution. The potential-flow solution is based on the first-order and second-order wave forces and hydrodynamic coefficients in frequency domain from WAMIT. The strip-theory loads include the distributed fluid inertia forces and viscous-drag forces using Morison’s equation, axial loads, static buoyancy loads, and lumped loads of ballast and marine growth.

In HydroDyn, the Morison forces are applied only along the portion of the member below the mean sea level. The wave kinematics within HydroDyn are only computed in the domain between the flat seabed and still-water level and thus no wave-kinematics stretching above mean water level is employed. The Morison equation is also applied for the mean platform position, so higher-order interaction between wave kinematics and body motion is not considered i.e., the Morison forces are applied at the original position of the structure instead of the instantaneous position.

## 2.6 FASTv8-OrcaFlex tool

Another commercial-level numerical simulation program, FASTv8-OrcaFlex, is also employed here for an extensive comparison purpose. Their coupling principle is similar to that of CHARM3D-FAST, i.e., (1) at each time step, FAST sends 6DOF motions and velocities to OrcaFlex; (2) OrcaFlex calculates added masses at the infinite frequency and hydrodynamic and mooring forces; (3) OrcaFlex sends these to FAST to solve the fully coupled matrix equation; (4) FAST solves the full equation of motion including platform’s 6DOFs and tower-servo-blade modes, which results in updated 6DOF displacements, velocities, and accelerations of the platform. The process is repeated in the next time step. As for the calculation of viscous drag forces on Morison members,

Table 5 Drag Coefficients for Morison members

|         | <b>Charm3D-FAST</b> | <b>OpenFAST</b>     | <b>FASTv8-OrcaFlex</b> |
|---------|---------------------|---------------------|------------------------|
| Column  | 1.6                 | 0.56 (main column)  | 0.56 (main column)     |
|         |                     | 0.61 (upper column) | 0.61 (upper column)    |
|         |                     | 0.68 (base column)  | 0.68 (base column)     |
| Brace   | 1.6                 | 0.63                | 0.63                   |
| Footing | 6.4                 | 9.6                 | 9.6                    |

Table 6 Natural frequencies ( $rad/s$ ) from the free-decay test

| <b>DOF</b> | <b>Charm3D-FAST</b> | <b>OpenFAST</b> | <b>FASTv8-OrcaFlex</b> | <b>Model Test</b> |
|------------|---------------------|-----------------|------------------------|-------------------|
| Surge      | 0.0556              | 0.0560          | 0.0552                 | 0.0555            |
| Heave      | 0.3605              | 0.3650          | 0.3621                 | 0.3641            |
| Pitch      | 0.2381              | 0.2402          | 0.2352                 | 0.2277            |

FASTv8-OrcaFlex is very similar to that of Charm3D-FAST. The OrcaFlex mooring dynamics model is based on a series of lumped masses connected by linear and torsional springs in contrast to the high-order rod FE model used in the Charm3D program.

### 3. Result and discussion

#### 3.1 Static offset test

First, to check the correct modeling of the mooring line and its static stiffness, surge offset tests were conducted by the two programs, Charm3D-Fast and OpenFAST, and the results are compared with the physical offset test done in the DeepCWind experiment, as shown in Fig. 6. They agree very well to each other to confirm that the surge system stiffness is correctly modeled. The correct system stiffness can also be observed from the match of natural frequencies among them in Table 6 and Fig. 7.

#### 3.2 Free-decay test

The free-decay test was numerically simulated by both Charm3D-FAST and OpenFAST for the comparison of the system's natural frequency and damping. The excitation loads and control mechanisms were switched off during the free-decay simulation. Table 5 shows the drag coefficients used in the numerical models. The hull viscous damping for surge mostly comes from the columns. The surge drag coefficient in Charm3D-FAST is larger than that used in other programs considering the scale effect (exaggeration of viscous effect in low Reynolds number). The footing of each column dominates the heave damping. The inertia and drag forces on braces are calculated by Morison equation since they were not included in the WAMIT discretization. The natural frequencies of the surge and heave simulations in both Charm3D-FAST and OpenFAST are almost the same as experimental results, as shown in Table 6 and Fig. 7. The simulated pitch natural frequencies are consistent between Charm3D-FAST and OpenFAST but they are slightly off compared to the measurements, which may be caused by the slight mismatch of mass distribution and center of

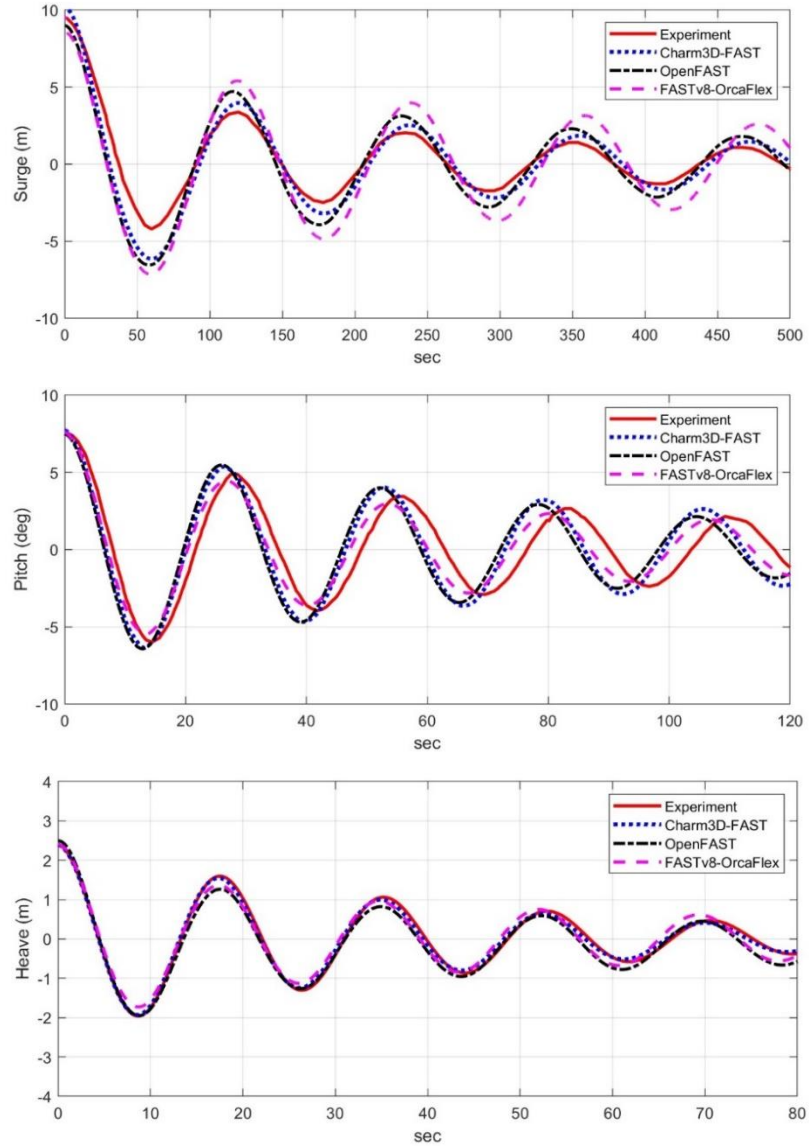


Fig. 7 Surge (Top), pitch (Middle), and heave (Bottom) free decay results

gravity during the model test. Observing the free-decay results in Fig. 7, the numerically simulated damping is very similar to the measured damping in the surge, heave, and pitch modes.

### 3.3 Case 1: White-noise wave-spectrum case ( $H_s = 7.1 \text{ m}$ , $T_p = 12.1 \text{ s}$ )

A white noise wave spectrum with  $H_s = 7.1 \text{ m}$  and  $T_p = 12.1 \text{ s}$  was used in the DeepCWind experiment and the same wave spectrum was inputted into Charm3D-FAST and OpenFAST. In the

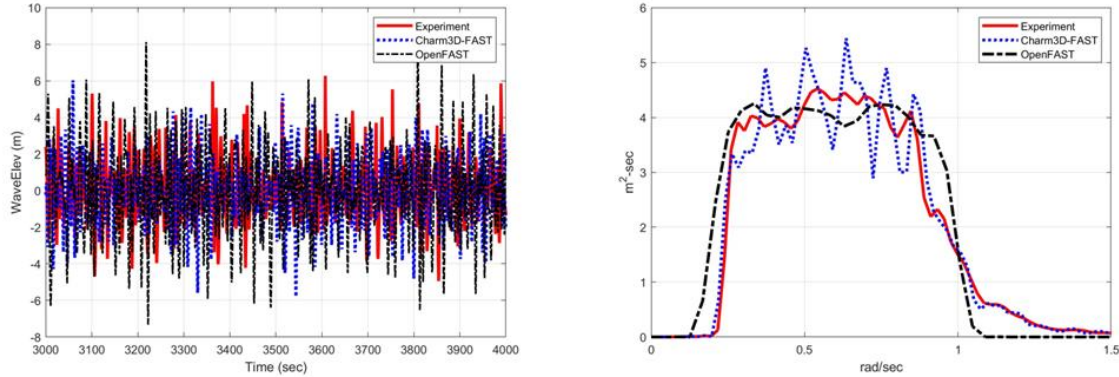


Fig. 8 Case 1 wave elevation time series (Left) and wave spectra (Right)

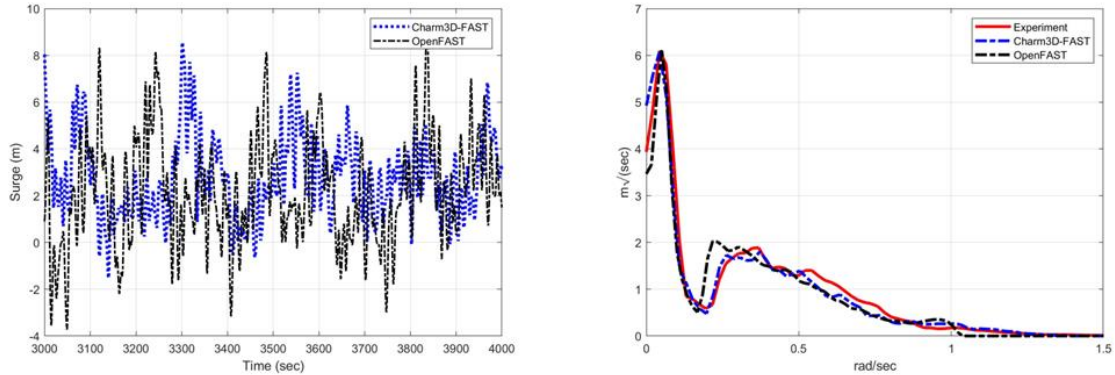


Fig. 9 Case 1 surge time series (Left) and spectra (Right) comparisons between simulated and experimental results

Charm3D-FAST, 100 wave components were employed using equal frequency intervals with random perturbed component central frequencies to avoid signal repetition when generating long time series. In OpenFAST, 1300 component waves were used with equally spaced frequency intervals and IFFT (inverse fast Fourier transform). In FASTv8-OrcaFlex, 500 component waves were used with equal-energy (variable) frequency intervals. In all three programs, the minimum and maximum cut-off frequencies were 0.2 and 2.0 rad/s. The generated wave time series and spectra in the numerical models and experiment are compared in Fig. 8. Overall, the predicted and measured data agreed well to each other. We cannot use the identical input random wave since the random-wave generation schemes of the respective programs are different. The Charm3D-FAST spectrum value near the pitch natural frequency ( $\sim 0.23$  rad/s) is a little bit smaller than the OpenFAST and measured ones, which is expected to contribute to the differences in the pitch peak amplitudes. There is no wave energy near the surge natural frequency of 0.055 rad/s. Therefore, the slowly varying surge motions near 0.055 rad/s are caused by the second-order difference-frequency wave loads including minor contributions from the nonlinear drag forces.

For fair comparisons among the three simulation programs, the same linear wave force, second-order difference-frequency wave force, and hydrodynamic and hydrostatic coefficients calculated

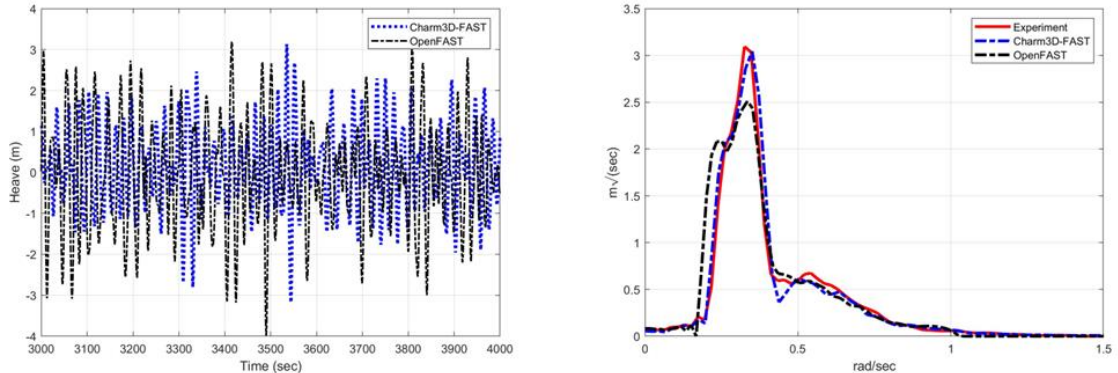


Fig. 10 Case 1 heave time series (Left) and spectra (Right) comparisons between simulated and experimental results

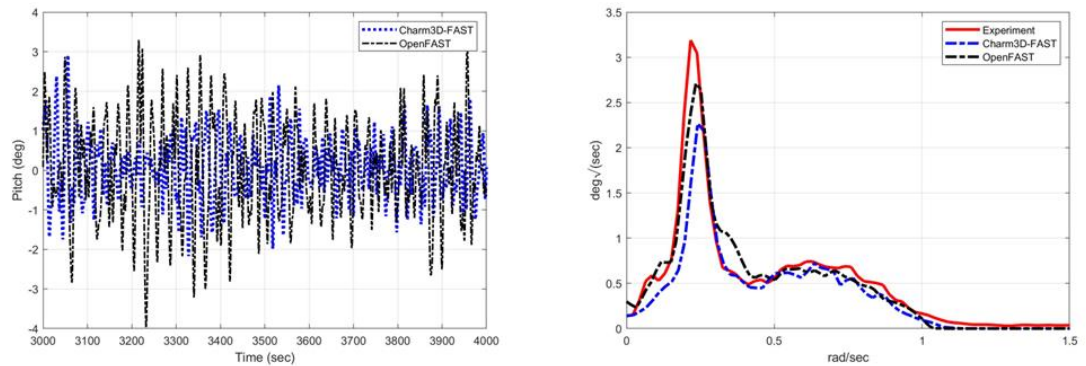


Fig. 11 Case 1 pitch time series (Left) and spectra (Right) comparisons between simulated and experimental results

from the WAMIT program were inputted. In all cases, 4000 s simulations were conducted and the 400 s–4000 s (1 hr) data are used for spectral and statistical calculations subtracting the initial 400 s as build-up time with the applied ramp function.

In Figs. 9–11, the surge/heave/pitch responses by the white-noise wave spectrum predicted by Charm3D-FAST and OpenFAST are compared with the experimentally measured values. In the case of surge, as expected, the slow-varying motions are dominant over the wave-frequency motions. Both numerical tools well recovered the physical surge responses.

In Fig. 10, the predicted heave motions are generally well-matched against the measured values. The heave peak amplitude of OpenFAST at its natural frequency ( $0.36 \text{ rad/s}$ ) is slightly worse than Charm3D-FAST when compared against the measured one. It may be attributed to the larger heave drag coefficient for column footing. However, the difference is small considering the variability caused by different random-wave realizations even by the same computer program.

In the case of pitch, the smaller peak amplitude by Charm3D-FAST compared to the experimental data is due to the smaller incident wave spectrum near  $0.25 \text{ rad/s}$  as shown in Fig. 8. The mooring-line tension is mainly affected by the surge and heave motions as demonstrated by the two peaks at surge and heave natural frequencies in Figs. 9 and 10. They are predicted well by both programs compared to the measured tension values.

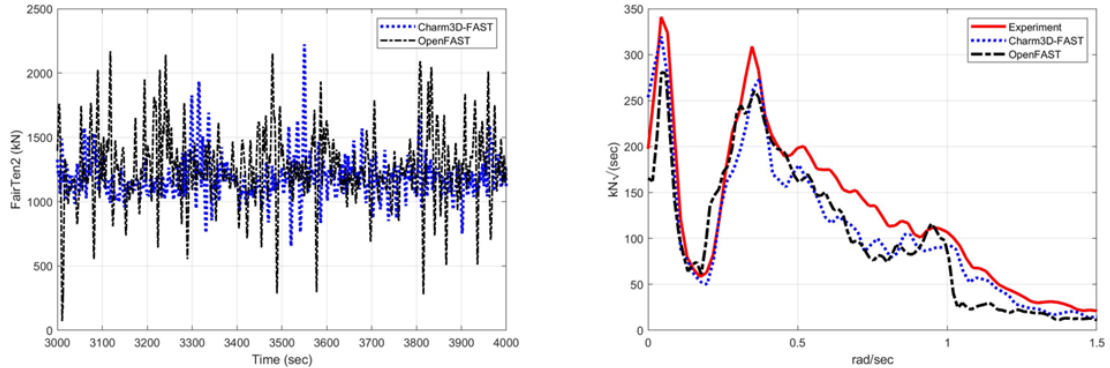


Fig. 12 Case 1 mooring line tension time series (Left) and spectra (Right) comparisons between simulated and experimental results

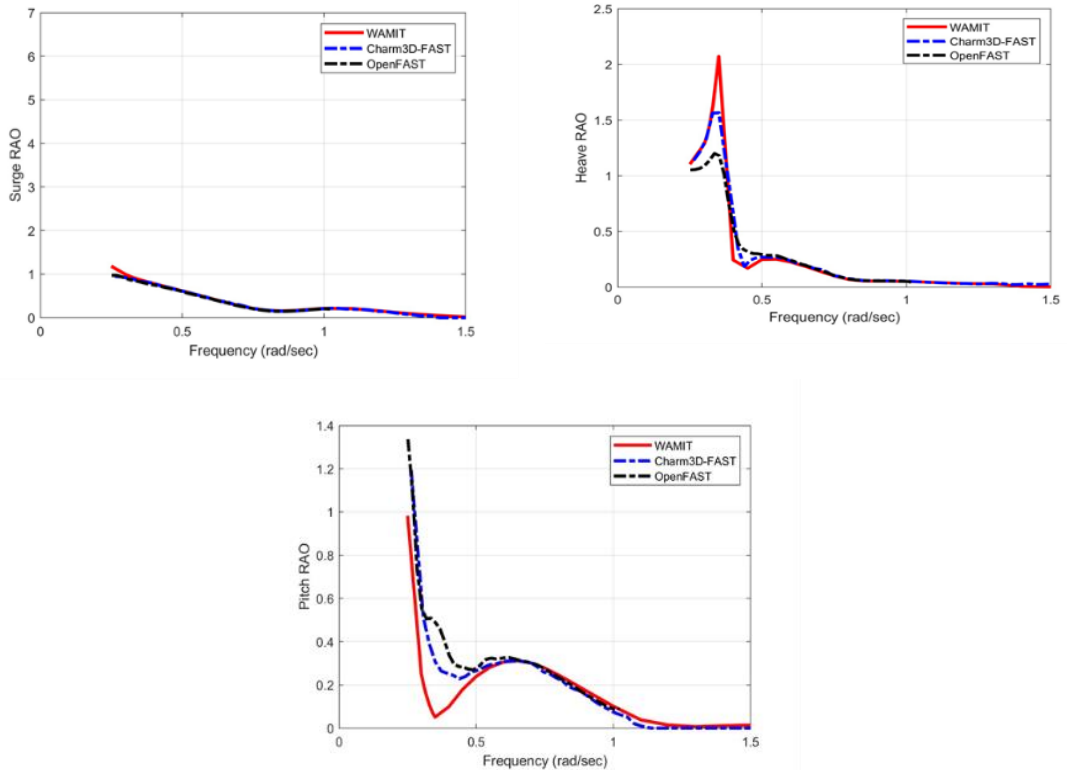


Fig. 13 Comparisons of surge (Top-left), heave (Top-right), and pitch (Bottom) RAOs from frequency-domain WAMIT calculation and regenerated RAOs from the time-domain simulations

Using the time-domain motion simulations, as was done in Figs. 9-11, the surge-heave-pitch RAOs can be reconstructed from the square root of motion spectrum to wave spectrum ratio. Then, they were compared with the original linear-potential-theory-based RAOs obtained from frequency-domain WAMIT program in Fig. 13. Due to the nonlinear and viscous effects imposed in the time-

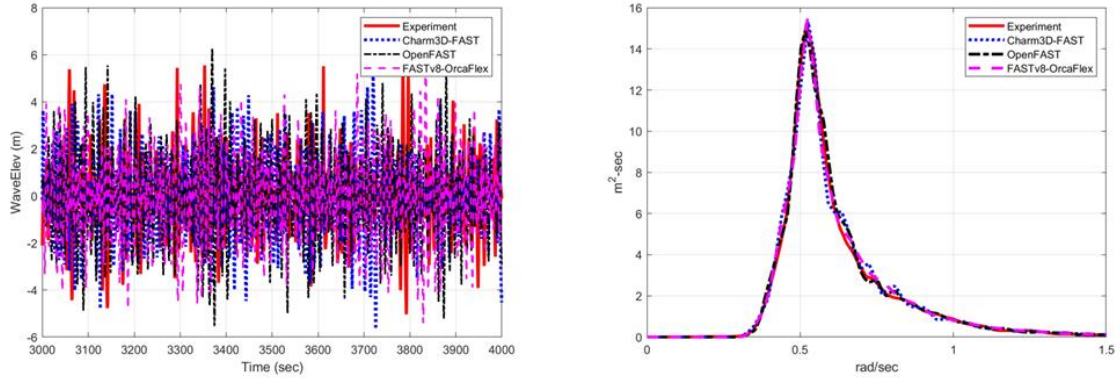


Fig. 14 Case 2 wave elevation time series (Left) and wave spectra (Right)

domain simulation, the regenerated RAOs from the simulations cannot be identical to the frequency-domain WAMIT results. However, there exist good agreements for the overall trends among them. We cannot obtain the RAOs outside the white-noise spectrum since there is no incident wave energy there and cannot be divided by zero.

### 3.4 Case 2: Irregular wave condition ( $H_s = 7.1 \text{ m}$ , $T_p = 12.1 \text{ s}$ )

Next, we conduct a similar analysis for more realistic irregular wave condition with the same significant wave height = 7.1 m and peak period = 12.1 s. In this section, we also introduced another result from the commercial-level program FASTv8-OrcaFlex. Fig. 14 demonstrates the wave elevations in the physical experiment and simulated by Charm3D-FAST, OpenFAST, and FASTv8-OrcaFlex and the corresponding power spectra, which match well between numerical simulations and experimental measurements.

The dynamic responses computed by the three different computer programs are plotted in Figs. 15-18 and they are compared with the experiment results. As shown in these figures, all the numerical results matched fairly well against the experimental results in the wave frequency range ( $\omega = 0.4\text{--}1.0 \text{ rad/s}$ ). However, there are nontrivial differences in the peak amplitudes for slowly varying surge and pitch responses caused by the second-order wave-force effects despite that the same WAMIT-produced second-order difference-frequency wave force QTFs are used. The low-frequency peaks are also influenced by the excitation and damping caused by nonlinear viscous drag force. There exists another uncertainty related to the variability of low-frequency peaks in 1-hour simulations depending on the selected random phases since there is a much smaller number of oscillations for the slowly-varying motions compared to the wave-frequency parts. The second-order low-frequency waves are also more difficult to dissipate in the wave tank causing more unwanted reflections. In this regard, we observe some discrepancies in the low-frequency peaks among the computer programs and experimental results.

In the case of heave motion as demonstrated in Fig. 16, both the Charm3D-FAST and OpenFAST results compare well with the field measurement. For the pitch responses shown in Fig. 17, the discrepancies between the numerical predictions and the experimental data become significant near the pitch natural frequency by similar reasons as the surge-response case and the slight shift of pitch natural frequencies among them. The discrepancy of the FASTv8-OrcaFlex is the largest in regard

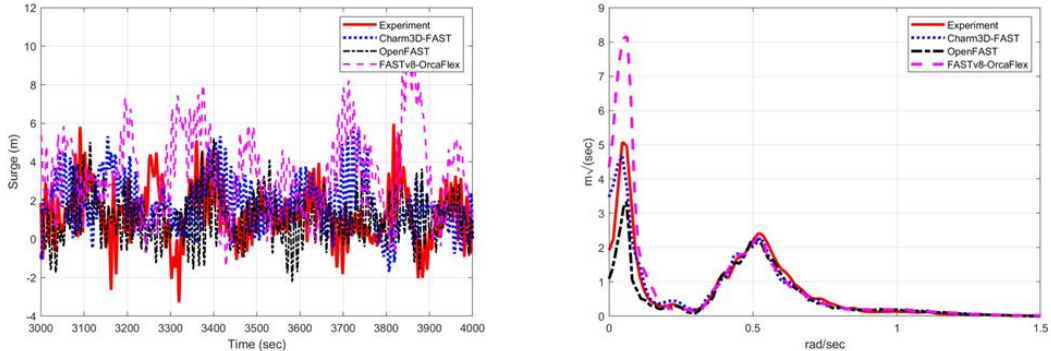


Fig. 15 Case 2 surge time series (Left) and spectra (Right) comparisons between simulated and experimental results

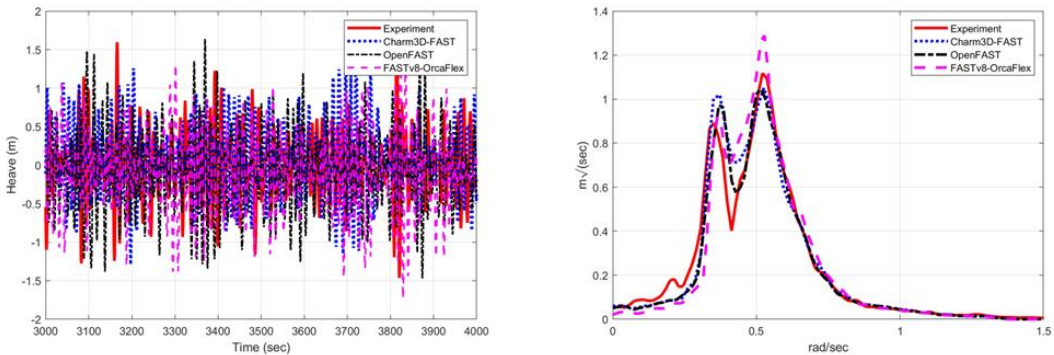


Fig. 16 Case 2 heave time series (Left) and spectra (Right) comparisons between simulated and experimental results

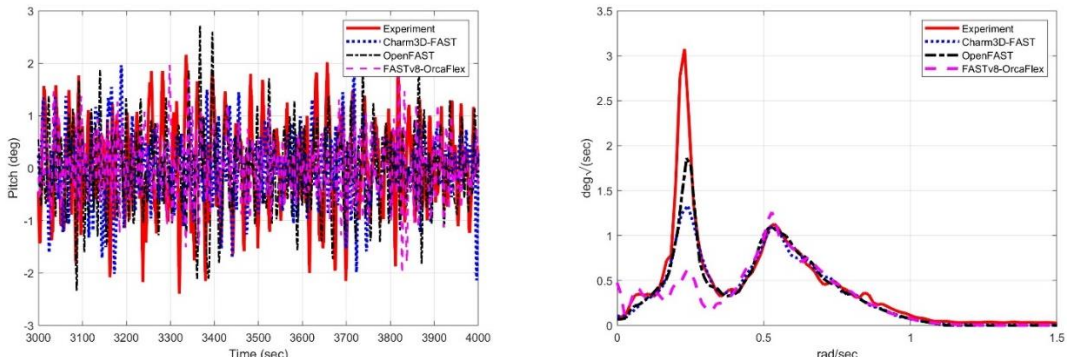


Fig. 17 Case 2 pitch time series (Left) and spectra (Right) comparisons between simulated and experimental results

to the pitch peak amplitude compared to the experimental value. The mooring tension is most affected by the surge and heave motions and thus its peaks are located at surge and heave natural frequencies, as shown in Figs. 15 and 16.

Table 7 Maximum (Max), minimum (Min), mean values, and standard deviation (STD) of the surge, heave, pitch of the floater and mooring tension

| DOF                | Program         | Max    | Min    | Mean  | STD   |
|--------------------|-----------------|--------|--------|-------|-------|
| Surge ( <i>m</i> ) | Experiment      | 7.256  | -3.285 | 1.244 | 1.495 |
|                    | Charm3D-FAST    | 7.199  | -2.294 | 1.950 | 1.464 |
|                    | OpenFAST        | 5.223  | -2.346 | 1.031 | 1.107 |
|                    | FASTv8-OrcaFlex | 11.080 | -3.926 | 3.312 | 2.237 |
| Heave ( <i>m</i> ) | Experiment      | 2.233  | -1.821 | 0.008 | 0.471 |
|                    | Charm3D-FAST    | 2.240  | -1.623 | 0.076 | 0.486 |
|                    | OpenFAST        | 1.641  | -1.548 | 0.082 | 0.468 |
|                    | FASTv8-OrcaFlex | 1.496  | -1.820 | 0.101 | 0.505 |
| Pitch (deg)        | Experiment      | 2.935  | -3.948 | 0.039 | 0.842 |
|                    | Charm3D-FAST    | 1.963  | -2.269 | 0.024 | 0.620 |
|                    | OpenFAST        | 2.728  | -2.336 | 0.005 | 0.673 |
|                    | FASTv8-OrcaFlex | 1.966  | -2.005 | 0.003 | 0.540 |
| Top Tension (kN)   | Experiment      | 2118   | 498    | 1214  | 142   |
|                    | Charm3D-FAST    | 2312   | 657    | 1201  | 140   |
|                    | OpenFAST        | 1682   | 550    | 1152  | 104   |
|                    | FASTv8-OrcaFlex | 2438   | 776    | 1279  | 190   |

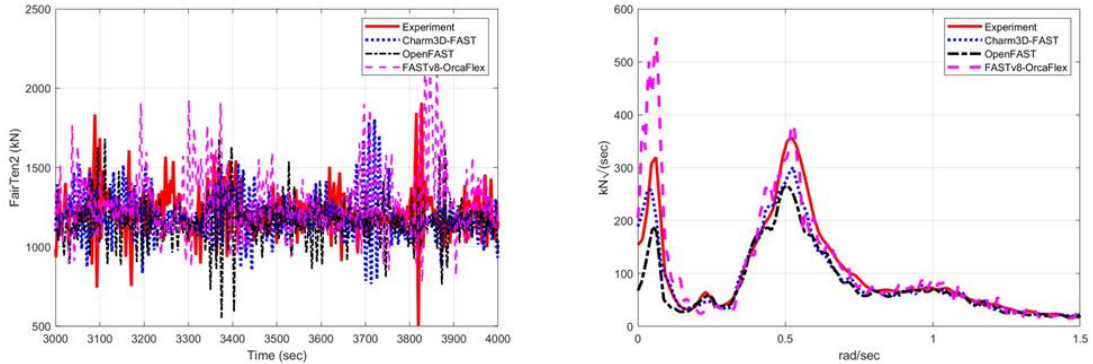


Fig. 18 Case 2 mooring line tension time series (Left) and spectra (Right) comparisons between simulated and experimental results

The corresponding statistics of Figs. 15-18 are summarized in Table 7. All the statistical results are obtained for time between 400 s and 4000 s, for the experiments and 3 programs. It is seen that the surge mean and maximum from FASTv8-OrcaFlex are appreciably overestimated while pitch standard deviations are underestimated, as can also be observed in the previous time series.

### 3.4 Case 3: Irregular wave condition with steady wind ( $H_s = 7.1 \text{ m}$ , $T_p = 12.1 \text{ s}$ , $W_s = 16.11 \text{ m/s}$ )

The third case we show here is with the addition of 16.11 m/s steady wind at the hub height to

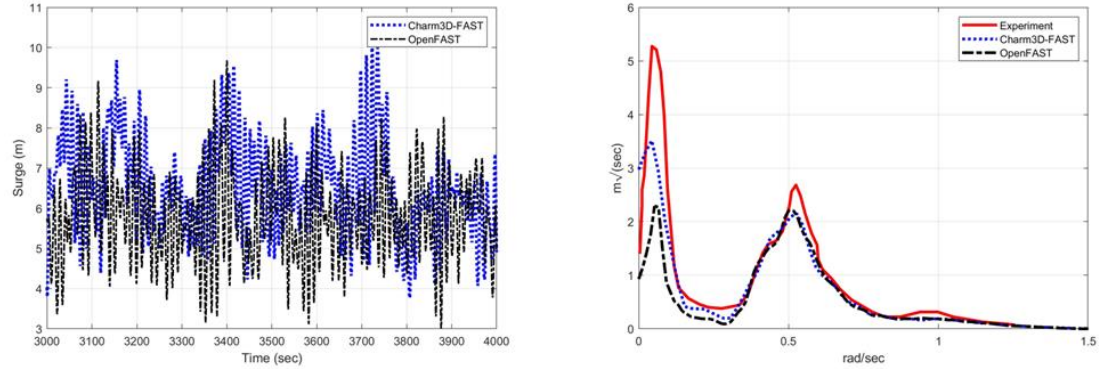


Fig. 19 Case 3 surge time series (Left) and spectra (Right) comparisons between simulated and experimental results

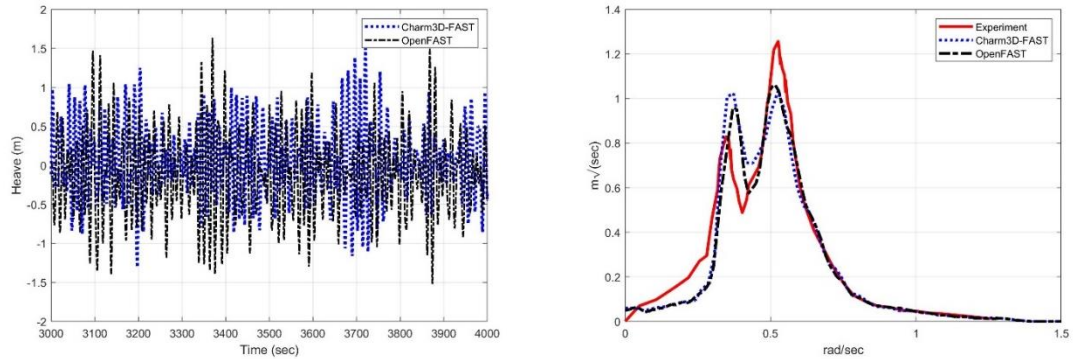


Fig. 20 Case 3 heave time series (Left) and spectra (Right) comparisons between simulated and experimental results

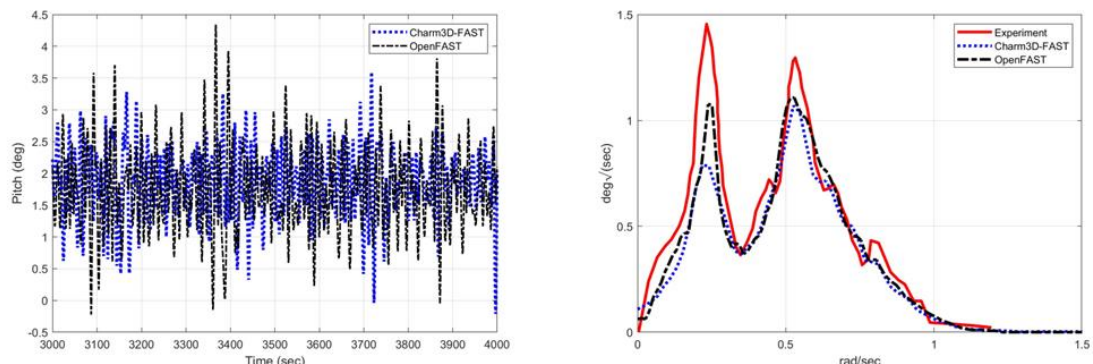


Fig. 21 Case 3 pitch time series (Left) and spectra (Right) comparisons between simulated and experimental results

the same irregular wave condition of the previous section i.e., the wave elevation time series and spectrum in the experiment and simulations are the same as in Fig. 14. In order for the same wind

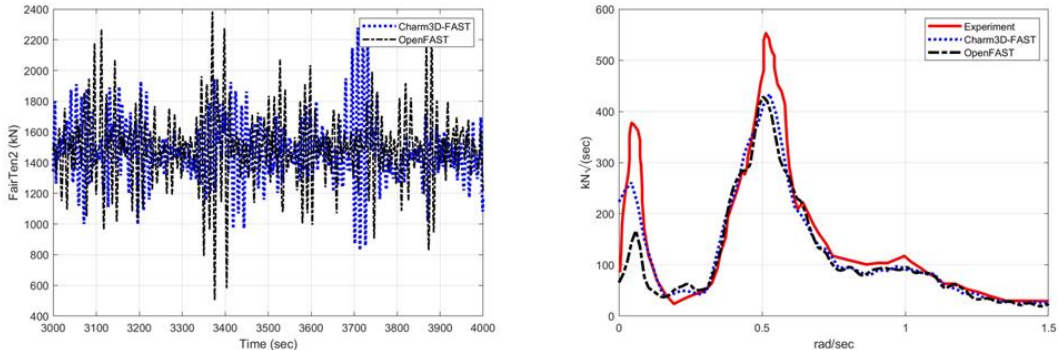


Fig. 22 Case 3 mooring line tension time series (Left) and spectra (Right) comparisons between simulated and experimental results

thrust to be given to the rotor as in the experiment, the blade pitch angle in the numerical simulations is fixed at 12.34 deg.

In Figs. 19–22, the results of the simulated motions (surge, pitch, and heave) and taut-side fairlead mooring tensions using Charm3D-FAST and OpenFAST are compared with the corresponding experimental values. Overall, their agreements look reasonably good, especially in the wave-frequency region. Compared to the above irregular-wave-only case, we observe greater discrepancies between the numerical and experimental results in the low-frequency region. This can be attributed to the less-than-perfect steady wind condition in the experiment since constant wind velocity is hard to be generated in the physical model testing. As a result of the steady wind applied, a surge mean offset of 6–7 m and a mean pitch angle of 2 degrees are generated, and thus mooring nonlinear effects (e.g., hardening) and the corresponding slight shift of surge natural frequency is to be more pronounced (Kim and Kim 2015), which can be observed in both simulation and measurement. The shift of mooring stiffness also influences the increase of wave-frequency mooring top tension. With the applied wind, aerodynamic damping is also introduced to affect the surge and pitch slowly-varying responses at the corresponding resonance peaks. The addition of steady horizontal wind has little influence on the heave motions.

#### 4. Conclusions

In the present study, we simulated the dynamic responses of a 5 MW OC4 semisubmersible-type wind turbine in various wave and wind conditions, as tested in the DeepCWind 1/50-scale experiment, by using the open-source numerical tool, OpenFAST and the in-house simulation tool, Charm3D-FAST. Their simulated results were consistently compared with the experimental results. Another commercial-level simulation tool, FASTv8-OrcaFlex was also employed for the selected cases of this comparative study. Three different environmental conditions, white-noise wave spectrum and realistic wave spectrum without and with steady wind were considered. In the simulations with 3 different programs, the same hydrodynamic coefficients and wave forces were calculated from the WAMIT second-order diffraction/radiation program and they were inputted to the respective simulation programs.

First, the system identification between the numerical and physical models was checked through

static offset test and free-decay test. The simulated system stiffness and damping agreed well with those of experiments. We then calculated the surge, heave, and pitch motions and the mooring line tensions of the offshore wind turbine in three different environments. From the comparisons, all the simulated results agreed reasonably well against the experimental results. The variabilities of surge and pitch resonant peak response amplitudes at low frequencies were larger than those of the wave-frequency responses due to significantly fewer number of oscillations and potential reflections of modulated long waves in the physical testing. From the comparative study, it can be concluded that the correctly modeled numerical simulation tools can well reproduce the complex coupled physics of floating wind turbines in random waves with and without steady winds. The differences among different simulation tools can be attributed to the differences in the modeling of nonlinear viscous drag forces, generating incident random waves, and other minor differences in the programming. Nevertheless, all the simulation tools correctly characterize the physical system and thus can be used as a digital twin of the physical system for further research. The present study also provides essential information pertaining to the development of the next generation larger-scale floating offshore wind turbines.

## References

- Bae, Y.H. and Kim, M.H. (2011), “Rotor-floater-mooring coupled dynamic analysis of mono-column-TLP-type FOWT (Floating Offshore Wind Turbine)”, *Ocean Syst. Eng.*, 1(1), 93-109. <https://doi.org/10.12989/ose.2011.1.1.095>.
- Bae, Y.H. and Kim, M.H. (2014), “Coupled dynamic analysis of multiple wind turbines on a large single floater”, *Ocean Eng.*, 92, 175-187. <https://doi.org/10.1016/j.oceaneng.2014.10.001>.
- Bae, Y.H. and Kim, M.H. (2014), “Influence of control strategy to FOWT global performance by aero-elastic-control-floater-mooring coupled dynamic analysis”, *Ocean Wind Energy*, 1(1), 50-58.
- Chen, J. and Kim, M.H. (2022), “Review of recent offshore wind turbine research and optimization methodologies in their design”, *Mar. Sci. Eng.*, 10(1), 28. <https://doi.org/10.3390/jmse10010028>.
- Coulling, A.J., Goupee, A.J., Robertson, A.N., Jonkman, J.M. and Dagher, H.J. (2013), “Validation of a FAST semi-submersible floating wind turbine numerical model with DeepCwind test data”, *Renew. Sust. Energ.*, 5, 023116. <https://doi.org/10.1063/1.4796197>.
- Coulling, A.J., Goupee, A.J., Robertson, A.N. and Jonkman, J.M. (2013), “Importance of second-order difference-frequency wave-diffraction forces in the validation of a fast semi-submersible floating wind turbine model”, *Proceedings of the 32th (2013) International Conference on Ocean, Offshore and Arctic Engineering Nantes, France*.
- Dominique, R., Christian, C., Alexia, A. and Alla, W. (2010), “WindFloat: A floating foundation for offshore wind turbines”, *Renew. Sust. Energ.*, 2, 033104. <https://doi.org/10.1063/1.3435339>.
- Jang, H.K., Park, S., Kim, M.H., Kim, K.H. and Hong, K. (2019), “Effects of heave plates on the global performance of a multi-unit floating offshore wind turbine”, *Renew. Energ.*, 134, 526-537. <https://doi.org/10.1016/j.renene.2018.11.033>.
- Jonkman, J.M. and Buhl Jr., M.L. (2004), “FAST user’s guide”, National Renewable Energy Laboratory, Rept. NREL/EL-500-29798, Golden, Colorado.
- Jonkman, J.M., Butterfield, S., Musial, W. and Scott, G. (2007), “Definition of a 5-MW reference wind turbine for offshore system development”, NREL Technical Report No. TP-500-38060.
- Kim, H.C. and Kim, M.H. (2015), “Global performances of a semi-submersible 5MW wind-turbine including second-order wave-diffraction effects”, *Ocean Syst. Eng.*, 5(3), 139-160. <https://doi.org/10.12989/ose.2015.5.3.139>.
- Kim, H.C. and Kim, M.H. (2016), “Comparison of simulated platform dynamics in steady / dynamic winds and irregular waves for OC4 semi-submersible 5MW wind-turbine against DeepCwind model-test results”,

- Ocean Syst. Eng.*, **6**(1), 1-21. <https://doi.org/10.12989/ose.2016.6.1.001>.
- Kim, H.C., Kim, M.H. and Choe, D.E. (2019), “Structural health monitoring of towers and blades for floating offshore wind turbines using operational modal analysis and modal properties with numerical-sensor signals”, *Ocean Eng.*, **188**, 106226. <https://doi.org/10.1016/j.oceaneng.2019.106226>.
- Kim, M.H., Ran, Z. and Zheng, W. (2001), “Hull/mooring coupled dynamic analysis of a truss spar in time domain”, *Int. J. Offshore Polar Eng.*, **11**(1), 42-54.
- Kim, M.H. and Yue, D.K.P. (1989), “The complete second-order diffraction solution for an axisymmetric body. Part 1. Monochromatic incident waves”, *J. Fluid Mech.*, **200**, 235-264. <https://doi.org/10.1017/S0022112089000649>.
- Kim, M.H. and Yue, D.K.P. (1990), “The complete second-order diffraction solution for an axisymmetric body. Part 2. Bichromatic incident waves and body motions”, *J. Fluid Mech.*, **211**, 557-593. <https://doi.org/10.1017/S0022112090001690>.
- Koo, B.J., Goupee, A.J., Kimball, R.W. and Lambrakos, K.F. (2014a), “Model tests for a floating wind turbine on three different floaters”, *J. Offshore Mech. Arct.*, **136**(2), 021904. <https://doi.org/10.1115/1.4024711>.
- Koo, B.J., Goupee, A.J., Lambrakos, K. and Lim, H.J. (2014b). “Model test data correlations with fully coupled hull/mooring analysis for a floating wind turbine on a semi-submersible platform”, *Proceedings of the 33th (2014) International Conference on Ocean, Offshore and Arctic Engineering, San Francisco*, USA.
- Li, C.X. and Zhang, J. (2016), “Nonlinear coupled dynamics analysis of a truss spar platform”, *China Ocean Eng.*, **30**(6), 835-850. <https://doi.org/10.1007/s13344-016-0054-2>.
- Masciola, M., Robertson, A.N., Jonkman, J.M., Alexander Coulling, A.J. and Goupee, A.J. (2013), “Assessment of the importance of mooring dynamics on the global response of the DeepCwind floating semisubmersible offshore wind turbine”, *Proceedings of the 23th International Offshore and Polar Engineering Conference, Anchorage*, USA.
- Tahar, A. and Kim, M.H. (2003), “Hull/mooring/riser coupled dynamic analysis and sensitivity study of a tanker-based FPSO”, *Appl. Ocean Res.*, **25**(6), 367-382. <https://doi.org/10.1016/j.apor.2003.02.001>.
- Yang, C.K. and Kim, M.H. (2010), “Transient effects of tendon disconnection of a TLP by hull-tendon-riser coupled dynamic analysis”, *Ocean Eng.*, **37**(8-9), 667-677. <https://doi.org/10.1016/j.oceaneng.2010.01.005>.
- Zhao, W. and Wan, D. (2015), “Numerical study of interactions between phase ii of oc4 wind turbine and its semi-submersible floating support system”, *J. Ocean Wind Energy*, **2**(1), 45-53.